



Generation of perversions in fibers with intrinsic curvature

Dandan Wang^{a,*}, M.D. Thouless^{a,b}, Wei Lu^{a,b}, J.R. Barber^b

^a Department of Material Science and Engineering, University of Michigan, Ann Arbor, MI 48109, USA

^b Department of Mechanical Engineering, University of Michigan, Ann Arbor, MI 48109, USA



ARTICLE INFO

Article history:

Received 10 October 2019

Revised 27 February 2020

Accepted 5 March 2020

Available online 9 March 2020

Keywords:

Fibers

Helix

Defects

Twist

Curvature

ABSTRACT

If a fiber is stretched, abraded on one side, and then gradually relaxed, it will deform into a helix. If the two ends are restrained from rotating during the relaxation, it will form two helical segments of opposite chirality separated by a perversion. Here we investigate the properties of the perversion using a finite-element solution, and show that an excellent approximation to both the shape and the associated strain energy can be obtained using a simple Rayleigh-Ritz approximation. The perversion deviates from the adjacent helices only in a relatively small region, which suggests the possibility of approximating more complex geometries by treating perversions as point defects.

Energetically, perversions are predicted only when they are 'geometrically necessary' because of the end restraint against rotation, but this energy differential is small when the fiber is almost straight and additional perversions can be generated by small perturbations. Some of these may approach and annihilate each other in pairs as the fiber is relaxed, but in other cases the additional perversions persist during unloading, despite the increased energy differential.

© 2020 Elsevier Ltd. All rights reserved.

1. Introduction

A recent experimental study of abrasion of non-woven fabrics (Wang et al., 2019) showed that the formation of pills was generally preceded by individual fiber damage in the form of waviness, twists, kinks and entanglements. Since in general only one side of the fiber is abraded, it seems reasonable to assume that the resulting inelastic deformation leads to a state of intrinsic curvature, and that these shapes are the response of the fiber structure to end constraints or loads.

A simple experiment that illustrates this is as follows: take a hair, a piece of fiber, or a ribbon, keep it taut, and use a finger nail to abrade one surface in a central segment. Now, relax the tension gradually. If the ends were allowed to rotate, the abraded segment would adopt a helical shape, but if they are prevented from rotating it will exhibit two helical segments of opposite chirality separated by a 'perversion' (Goriely and Tabor, 1998; McMillen and Goriely, 2002), as shown in Fig. 1.

Long, thin fibers play an important role in many natural and technological systems. Applications range from microstructures such as supramolecular helices (Yang et al., 2013), nanobelts (Gao et al., 2005), DNA (Mendelson, 1978), and polymer chains (Wie et al., 2015), to macro-structures including animal organs (Savin et al., 2011), plant tendrils (Gerbode et al., 2012; Goriely and Tabor, 1998; Wang et al., 2013), and cables (Goyal et al., 2005).

* Corresponding author.

E-mail addresses: dandanw@umich.edu (D. Wang), thouless@umich.edu (M.D. Thouless), weilu@umich.edu (W. Lu), jbarber@umich.edu (J.R. Barber).

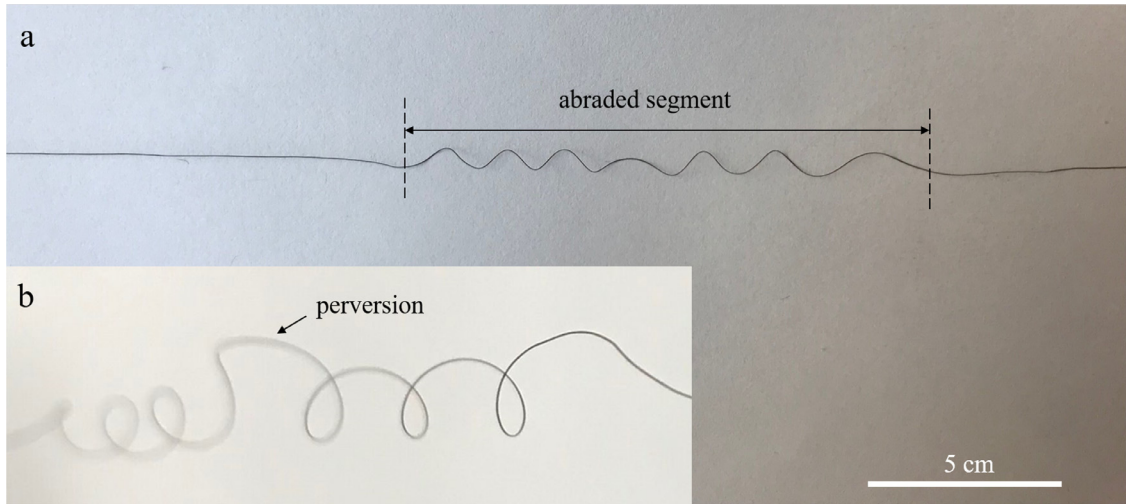


Fig. 1. (a) The shape of a fiber abraded in a central segment; (b) Enlarged perspective view of the abraded segment showing two helices separated by a perversion.

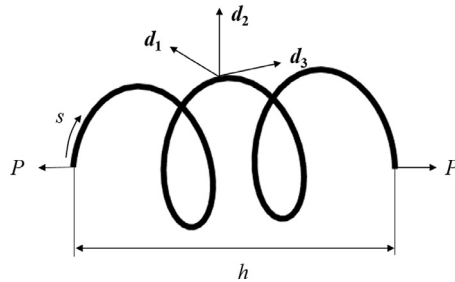


Fig. 2. A fiber loaded by equal and opposite forces at its ends. We define a path coordinate s and a director basis $\{\mathbf{d}_1(s), \mathbf{d}_2(s), \mathbf{d}_3(s)\}$. We also define the end-to-end distance h .

If a fiber is sufficiently long and thin, its deformation is dominated by bending and twisting, and can be described using the Kirchhoff equations (Callan-Jones et al., 2012; Goriely and Tabor, 1997; Olson et al., 2013). Analytical solutions exist for an infinitely long fiber under tension or compression without twist (van der Heijden et al., 2003), and for a fiber with uniform intrinsic curvature under tension deforming into a uniform helix (Goriely, 2017; Goriely and Tabor, 1998; McMillen and Goriely, 2002). If a fiber with intrinsic curvature is straightened and the ends are then prevented from rotating during unloading, the requirement that the end-to-end twist be zero causes it to form two equal helices of opposite chirality separated by a perversion, as shown in Fig. 1. This was recognized by Darwin, as explained by Pieranski et al. (2004). Domokos and Healey (2005) investigated and classified the equilibrium configurations for a fiber with intrinsic curvature. They showed that a state with a single perversion bifurcates stably from the straight configuration as the tension is reduced, and that there are equilibria involving multiple perversions. A more general computational approach for problems of this class was developed by Kumar and Healey (2010).

Goriely and coworkers (Goriely and Tabor, 1996; 1998; McMillen and Goriely, 2002) obtained an approximate description for the shape of a perversion by perturbing the solution for a straight fiber. In particular, they showed that this approach defines a shape that is asymptotically close to the corresponding pure helices. However, it is clear that the shape illustrated in Fig. 1, as well as those of fibers in abrasion experiments (Wang et al., 2019), do not generally meet the condition of being almost straight. Therefore, in this paper, we use finite-element solutions and Rayleigh-Ritz approximations to describe the shape of more relaxed fibers. We also show that the resultant shapes are very sensitive to small perturbations in the initial conditions and to the loading history.

2. Mathematical model

The Kirchhoff model provides a mathematical framework to describe the deformation of a thin fiber in bending and torsion. We assume that the fiber is inextensible, and define a path-length coordinate, s , such that the location of a point on the fiber is defined by the position vector $\mathbf{r}(s)$. We also define a director basis $\{\mathbf{d}_1(s), \mathbf{d}_2(s), \mathbf{d}_3(s)\}$, as shown in Fig. 2, such that $\mathbf{d}_3(s)$ is the unit vector in direction $\mathbf{r}'(s)$, where the prime denotes the derivative with respect to s . The unit vectors $\mathbf{d}_1(s)$ and $\mathbf{d}_2(s)$ are defined so as to align with the principal axes of the cross-section, for which the second moments of

area are I_1 and I_2 , respectively. The local curvature and twist of the fiber can be combined in a vector $\mathbf{k}(s)$, defined such that

$$\mathbf{d}_i' = \mathbf{k} \times \mathbf{d}_i; \quad i = 1, 2, 3. \quad (1)$$

In the unloaded state, the shape of the fiber is defined by an intrinsic curvature vector $\mathbf{k}^{(0)}(s) = \{k_1^{(0)}, k_2^{(0)}, k_3^{(0)}\}$.

We consider the case where the fiber is loaded only at the ends by equal and opposite forces P . In this case the equilibrium of internal force $\mathbf{F}(s)$ and moment $\mathbf{M}(s)$ leads to the quasistatic Kirchhoff equations

$$\mathbf{F}' = \mathbf{0}; \quad \mathbf{M}' + \mathbf{d}_3 \times \mathbf{F} = \mathbf{0} \quad (2)$$

(McMillen and Goriely, 2002). The moment $\mathbf{M}(s)$ is related to the local curvature $\mathbf{k}(s)$ by the constitutive relation

$$\mathbf{M} = EI_1(k_1 - k_1^{(0)})\mathbf{d}_1 + EI_2(k_2 - k_2^{(0)})\mathbf{d}_2 + GK(k_3 - k_3^{(0)})\mathbf{d}_3, \quad (3)$$

where E is Young's modulus, G is the shear modulus, and K is the torsional stiffness. If this is substituted into Eq. (2), it is clear that we will have six ordinary differential equations for the six unknowns k_1, k_2, k_3, F_1, F_2 and F_3 .

2.1. Dimensionless formulation

It is convenient to introduce dimensionless measures, \tilde{s} , $\tilde{\mathbf{F}}$, \tilde{P} , $\tilde{\mathbf{M}}$ and $\tilde{\mathbf{k}}$, through the definitions

$$s = \tilde{s}/k_0; \quad \mathbf{F} = \tilde{\mathbf{F}}EI_1k_0^2; \quad P = \tilde{P}EI_1k_0^2; \quad \mathbf{M} = \tilde{\mathbf{M}}EI_1k_0; \quad \mathbf{k} = \tilde{\mathbf{k}}k_0, \quad (4)$$

where k_0 is an appropriate scalar measure of intrinsic curvature or twist. Since the numerical calculations that we discuss later are dynamic in nature, we will also introduce a non-dimensional form, \tilde{t} , for time

$$t = \tilde{t}L\sqrt{E/\rho}, \quad (5)$$

where ρ is the density of the fibers.

The Kirchhoff Eq. (2) retain the same form with the normalization of the parameters, and the constitutive relation reduces to

$$\tilde{\mathbf{M}} = (\tilde{k}_1 - \tilde{k}_1^{(0)})\mathbf{d}_1 + \Lambda(\tilde{k}_2 - \tilde{k}_2^{(0)})\mathbf{d}_2 + \Gamma(\tilde{k}_3 - \tilde{k}_3^{(0)})\mathbf{d}_3, \quad (6)$$

where $\Lambda = I_2/I_1$ and $\Gamma = GK/EI_1$.

From the equilibrium Eq. (2) and the constitutive law (6), we can obtain a relationship between k_1, k_2 and k_3 :

$$\Gamma(\tilde{k}_3' - \tilde{k}_3^{(0)'}) - (\tilde{k}_1 - \tilde{k}_1^{(0)})\tilde{k}_2 + \Lambda(\tilde{k}_2 - \tilde{k}_2^{(0)})\tilde{k}_1 = 0, \quad (7)$$

where the prime now represents the derivative with respect to \tilde{s} .

In this paper, we restrict attention to incompressible fibers of circular cross-section with uniform intrinsic curvature, so that

$$\mathbf{k}^{(0)} = \{k_1^{(0)}, 0, 0\}; \quad \Lambda = 1; \quad \Gamma = \frac{2}{3}. \quad (8)$$

If we further choose $k_0 = k_1^{(0)}$,

$$\tilde{k}_3' = -\frac{3}{2}\tilde{k}_2, \quad (9)$$

and the problem is completely characterized by the dimensionless parameters \tilde{P} and $k_1^{(0)}L$, where L is the length of the fiber.

In this paper, we will also use the result that the elastic strain energy per unit length, U , is given by

$$\tilde{U} \equiv \frac{U}{EI_1k_0^2} = \frac{1}{2}(\tilde{k}_1 - 1)^2 + \frac{1}{2}\tilde{k}_2^2 + \frac{1}{3}\tilde{k}_3^2. \quad (10)$$

2.2. Uniform helix solution

If the ends of a long fiber are pulled apart by a force P , and are not restrained against rotation, the fiber forms a uniform helix except for a region near the ends. The dimensionless curvature \tilde{k}_1 and twist \tilde{k}_3 of a pure helix are independent of \tilde{s} , and hence $\tilde{k}_2 = 0$ from Eq. (9).

The shape of the helix is defined by two parameters: a length scale such as the pitch p or the coil radius r , and a dimensionless parameter which could be any one of the helix angle α , the ratio p/r or h/L , where the end-to-end distance h is defined in Fig. 2. Here the curvature k_1 and twist k_3 are chosen as the two parameters, in terms of which (O'Neill, 2006),

$$\hat{h} = \frac{h}{L} = \frac{k_3}{\sqrt{k_1^2 + k_3^2}}. \quad (11)$$

This equation retains the same form when it is expressed in terms of the non-dimensional parameters \tilde{k}_1, \tilde{k}_2 and \tilde{k}_3 .

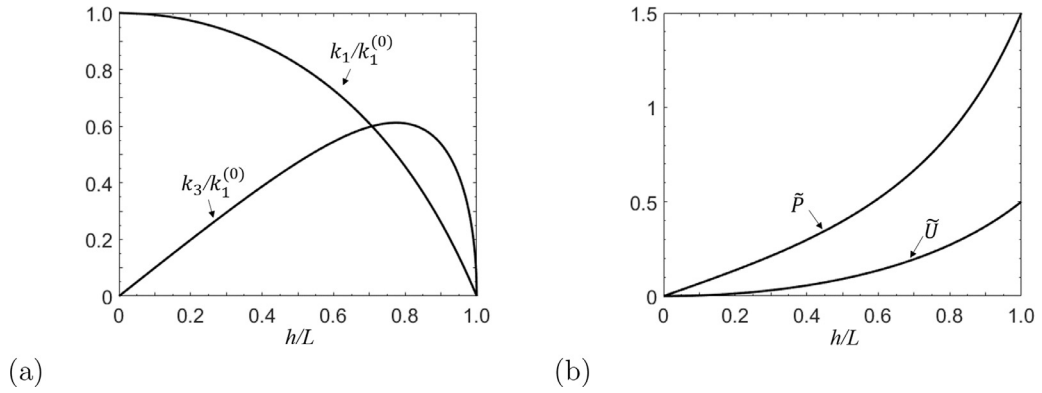


Fig. 3. (a) Normalized curvature \tilde{k}_1 and twist \tilde{k}_3 , and (b) force \tilde{P} and strain energy \tilde{U} for a uniform helix as functions of end-to-end distance h/L .

The total energy per unit length Π consists of the strain energy, U , and the potential energy, $-Ph/L$, of the applied force P . The dimensionless total energy for the uniform helix is therefore (Goriely and Tabor, 1998):

$$\tilde{\Pi} = \tilde{U} - \tilde{P}\tilde{h} = \frac{1}{2}(\tilde{k}_1 - 1)^2 + \frac{1}{3}\tilde{k}_3^2 - \tilde{P}\tilde{h} \quad (12)$$

from Eq. (10). An equilibrium configuration is one that minimizes the total energy, with

$$\frac{d\tilde{\Pi}}{d\tilde{k}_1} = 0; \quad \frac{d\tilde{\Pi}}{d\tilde{k}_3} = 0. \quad (13)$$

These equations permit all the dimensionless parameters to be expressed in terms of \tilde{k}_1 , and we obtain

$$\tilde{P} = \sqrt{\frac{(1 - \tilde{k}_1)(3 - \tilde{k}_1)^3}{12}}; \quad \tilde{k}_3 = \sqrt{\frac{3}{2}(\tilde{k}_1 - \tilde{k}_1^2)}; \quad \tilde{U} = \frac{1 - \tilde{k}_1}{2} \quad (14)$$

(McMillen and Goriely, 2002). The relations between the normalized curvature, \tilde{k}_1 , twist, \tilde{k}_3 , force, \tilde{P} , strain energy, \tilde{U} , and the end-to-end distance, \tilde{h} , are plotted parametrically in Fig. 3.

3. Shape of the perversion

When the tensile force at the end of the fiber is zero, it forms a coil in a plane. Then, as mentioned previously, after the fiber has been pulled into a straight configuration, and the rotation of the ends is prevented as the force P is reduced again, the fiber deforms into two similar helices of opposite handiness separated by a perversion, as shown in Fig. 1. If h/L is only slightly less than unity, an analytical approximation to the shape of the perversion can be obtained by perturbation methods (McMillen and Goriely, 2002). For lower values of h/L , a numerical solution must be used. We will also demonstrate the use of a Rayleigh-Ritz approach in the next section.

Finite-element simulations were conducted using the software 'ABAQUS/Explicit' with elastic-beam elements.¹ The ratio between the fiber diameter and length was chosen to be very small (10^{-3}), in order to render extensional effects negligible. Automatic time increments and a small damping coefficient were used. A Python script was written to establish the shape of fiber by integrating the curvature. The initial set of numerical results that will be presented were obtained under quasi-static conditions, for which the kinetic energy was always negligible compared to the strain energy. This condition was relaxed in a subsequent set of calculations conducted to explore the effects of rate and noise on the formation of perversions.

To test the accuracy of the finite-element solutions, we allowed end rotation so that the shape was a pure helix, except near the ends. The strain energy of a central helical segment is compared to that of the analytical solution in Fig. 4, and shows excellent agreement. Notice that in this figure, and throughout this section, we present results as functions of h/L in a helical segment rather than as functions of the force \tilde{P} , since values for h/L show less uncertainty than those for \tilde{P} in the finite-element solutions. The two parameters are related through Eqs. (11) and (14), which can be solved to give

$$\tilde{P} = \frac{6h/L}{(3 - h^2/L^2)^2}. \quad (15)$$

Fig. 5 shows two views of the shape of a perversion generated in ABAQUS for the case where $h/L = 0.78$ for the adjacent helical segments. However, it is easier to characterize the properties of the perversion by plotting \tilde{k}_1 , \tilde{k}_2 and \tilde{k}_3 as functions of \tilde{s} . Fig. 6(a) shows this plot for $h/L = 0.88$, where the finite-element results are plotted as points. The curvatures \tilde{k}_1 , \tilde{k}_2

¹ A mesh size of about $0.03k_1^{(0)}$ was used, but a reasonable level of insensitivity to this choice was verified. A similar insensitivity to the choice of damping coefficient was also verified by using values of 0.06 and 0.6. Unless specified otherwise, $d\tilde{h}/d\tilde{t} = 9.7 \times 10^{-7}$ so as to ensure quasi-static conditions.

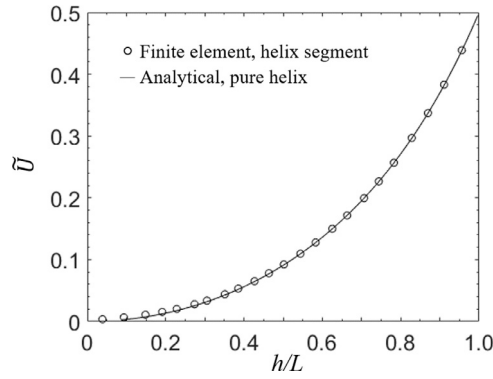


Fig. 4. The normalized strain energy of a helix segment as a function of the end-to-end distance from finite-element calculations (points) and the analytical solution from Eqn. 14 (line). The numerical uncertainties in this plot are smaller than the data points.

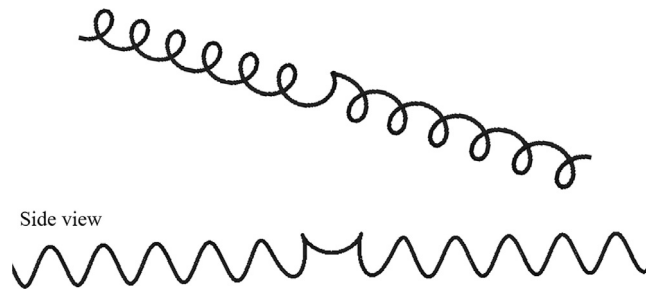


Fig. 5. Two views of a typical ABAQUS output showing helical coils of opposite chirality separated by a perversion. $h/L = 0.78$.

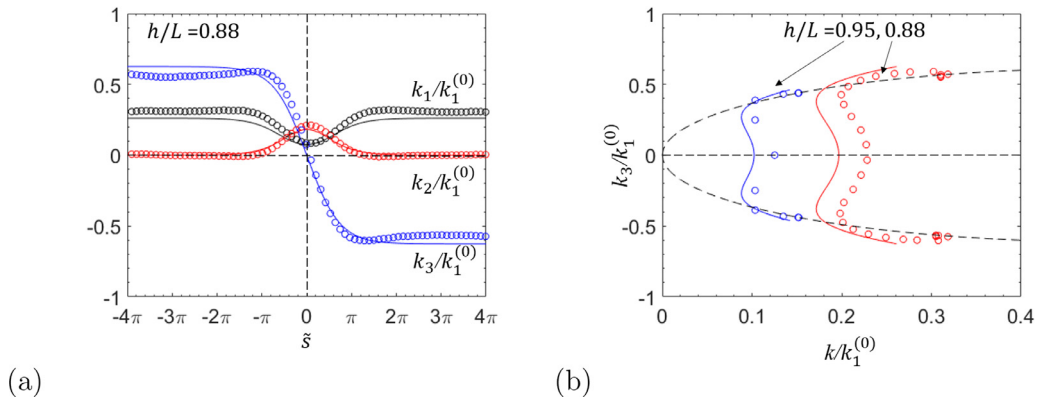


Fig. 6. (a) Finite-element results (points) for \tilde{k}_1 , \tilde{k}_2 and \tilde{k}_3 in the perversion segment as functions of \bar{s} for $h/L = 0.88$. The solid lines are obtained from McMillan and Goriely's perturbation solution for a value of $\mu = -0.19$, corresponding to $h/L = 0.88$. (b) The same results plotted in $\tilde{k}_3 - \tilde{k}$ space, where $\tilde{k} = \sqrt{\tilde{k}_1^2 + \tilde{k}_2^2}$. The dashed line represents the locus of fixed points defined by the pure helix relation (14)₂. We also present a similar comparison for $h/L = 0.95$ (corresponding to $\mu = -0.095$), for which the agreement with the perturbation solution is much closer. The numerical uncertainties in this plot are smaller than the data points.

are symmetric about the midpoint of the perversion, whereas the twist \tilde{k}_3 is anti-symmetric. The finite-element results tend asymptotically to the appropriate values of a pure helix away from the mid-point of the perversion, and the decay is fairly rapid, implying that the form of the perversion is not influenced by the necessarily finite length of the fiber. There is also a noticeable 'overshoot' implying oscillatory decay, particularly in the results for \tilde{k}_3 .

For comparison, the solid lines in Fig. 6(a) were obtained using McMillan and Goriely's perturbation solution (McMillan and Goriely, 2002). However, we note that the corresponding value of their parameter $\mu = -0.19$, equivalent to $h/L = 0.88$, is outside the range in which they would claim the perturbation procedure provides a good approximation. In particular, the perturbation solution does not capture the oscillatory decay observed in the numerical results.

In Fig. 6(b), the same results are plotted in $\tilde{k}_3 - \tilde{k}$ space, where $\tilde{k} = \sqrt{\tilde{k}_1^2 + \tilde{k}_2^2}$ is the magnitude of the curvature. The dashed line represents the locus of fixed points defined by the relationship for a pure helix (Eq. (14)). In this figure, we also show the same comparison for $h/L = 0.95$ ($\mu = -0.095$), confirming that the perturbation solution gives a much better fit as h/L approaches unity.

3.1. Rayleigh–Ritz approximation to the shape

In their bifurcation analysis to determine the stability of small perturbations from the straight configuration, Domokos and Healey (2005) define a vector of labels $w_i \in \{-1, 0, 1\}$, each component of which essentially characterizes the chirality of a helical segment comprising a single coil of the initial undeformed fiber. The sequence of values, w_i , then defines the approximate shape of the deformed fiber, and, in particular, perversions are identifiable as locations where adjacent segments have opposite values of w_i . In our formulation, the chirality of a fiber segment is defined by $\text{sgn}(\tilde{k}_3(\tilde{s}))$ and a closely related approximation to the shape could be defined by representing $\tilde{k}_3(\tilde{s})$ as a piecewise constant function. This is equivalent to idealizing the perversion as a point defect, which could lead to useful simplifications in the investigation of more complex patterns. There are clear parallels here with dislocations, and in particular with geometrically necessary dislocations (Arsenlis and Parks, 1999; Nye, 1953), since we have already remarked that at least one perversion must exist under the conditions of loading such as those in Fig. 1.

However, a step function in $\tilde{k}_3(\tilde{s})$ implies a locally infinite value of $\tilde{k}_2(\tilde{s})$ from Eq. (8), and hence implies a non-integrable singularity in strain-energy density. Of course, a similar problem is encountered with a discrete dislocation, and it can be avoided by using an appropriate regularization. For example, in the Peierls–Nabarro dislocation model (Joos and Duesbery, 1997), the relative displacement of the two halves of the crystal is approximated by an arctan function. In the next section, we shall propose appropriate regularizations for the functions $\tilde{k}_1(\tilde{s})$, $\tilde{k}_2(\tilde{s})$, $\tilde{k}_3(\tilde{s})$ near a perversion, and determine the values of the corresponding parameters using the Rayleigh–Ritz method.

3.1. Rayleigh–Ritz approximation to the shape

The results in Fig. 6 suggest that the functions $\tilde{k}_1(\tilde{s})$, $\tilde{k}_2(\tilde{s})$ might be approximated by

$$\tilde{k}_1(\tilde{s}) = a_1 \exp(-b_1 \tilde{s}^2) \cos(c_1 \tilde{s}) + \tilde{k}_1^{\text{helix}}(\hat{h}) \quad (15)$$

$$\tilde{k}_2(\tilde{s}) = a_2 \exp(-b_2 \tilde{s}^2) \cos(c_2 \tilde{s}), \quad (16)$$

where $\tilde{k}_1^{\text{helix}}(\hat{h})$ corresponds to the uniform helix value plotted in Fig. 3(a) and a_1 , b_1 , c_1 , a_2 , b_2 , c_2 are parameters to be determined. These expressions tend asymptotically to the uniform helix values from Eqs. (10) and (13) with increasing $|\tilde{s}|$.

Eq. (9) can be integrated to give

$$\tilde{k}_3(\tilde{s}) = -\frac{3}{2} \int_0^{\tilde{s}} \tilde{k}_2(\tilde{s}) d\tilde{s} = -\frac{3\sqrt{\pi}a_2}{4\sqrt{b_2}} \exp\left(-\frac{c_2^2}{4b_2}\right) \Re\left\{\text{erf}\left(\sqrt{b_2}\tilde{s} + \frac{ic_2}{2\sqrt{b_2}}\right)\right\}, \quad (17)$$

and, since $\tilde{k}_3(\tilde{s})$ must tend to the limiting value $\tilde{k}_3^{\text{helix}}(\hat{h})$ as $|\tilde{s}| \rightarrow \infty$, we obtain

$$a_2 = -\frac{4\sqrt{b_2}\tilde{k}_3^{\text{helix}}(\hat{h})}{3\sqrt{\pi} \exp(-c_2^2/4b_2)}, \quad (18)$$

which reduces the number of free parameters (degrees of freedom) in Eqs. (15)–(17) to five (a_1 , b_1 , c_1 , b_2 , c_2).

The Rayleigh–Ritz approximation is then obtained by substituting these trial functions into Eq. (10), integrating with respect to \tilde{s} , and then minimizing the total energy $\tilde{\Pi}$ with respect to the free parameters. We used the MatLab ‘fminsearch’ package which is based on the Nelder–Mead simplex direct-search algorithm. If the variation of the shape of the perversion is tracked as the tensile force, \tilde{P} , or the end-to-end length, h/L , is reduced, it is efficient to use the values of the parameters at the previous step as an initial guess for the search algorithm. Computationally, the Rayleigh–Ritz algorithm is about 100 times faster than the direct finite-element solution.

Fig. 7 compares the Rayleigh–Ritz approximation (solid lines) with finite-element results (points) for $h/L = 0.88$ and 0.78. The agreement is clearly excellent, and this is confirmed by a comparison of the three-dimensional shapes for $h/L = 0.78$ in Fig. 8.

3.1.1. Lower values of h/L

The Rayleigh–Ritz approximation of Eqs. (15)–(17) provides a good fit to the finite-element results in the range $0.65 < h/L < 1$, but significant errors are obtained for lower values. Fig. 9(a) compares the solutions for $h/L = 0.32$. It can be seen that the finite-element results exhibit several cycles of oscillation that are not captured by the Rayleigh–Ritz solution, and the asymptotic approach to the helix value is slower. This should be compared to the good agreement seen at larger values of h/L in Fig. 7.

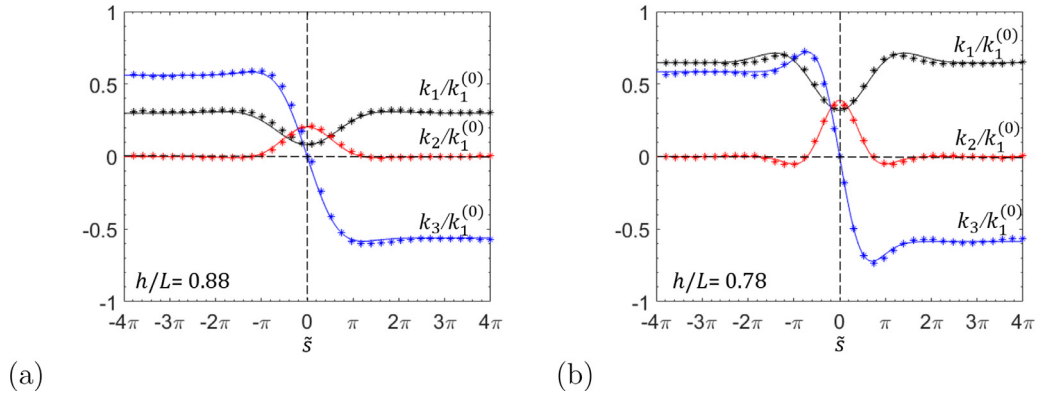


Fig. 7. Rayleigh-Ritz approximations with five parameters for the curvature and twist functions \tilde{k}_1 , \tilde{k}_2 and \tilde{k}_3 (lines) compared with finite element results (points) for (a) $h/L = 0.88$ and (b) $h/L = 0.78$. The numerical uncertainties in these plots are smaller than the data points.

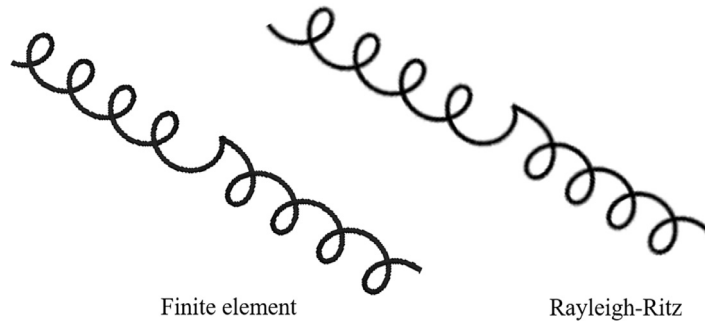


Fig. 8. Comparison of the predicted fiber morphology from finite element and Rayleigh-Ritz calculations for $h/L = 0.78$.

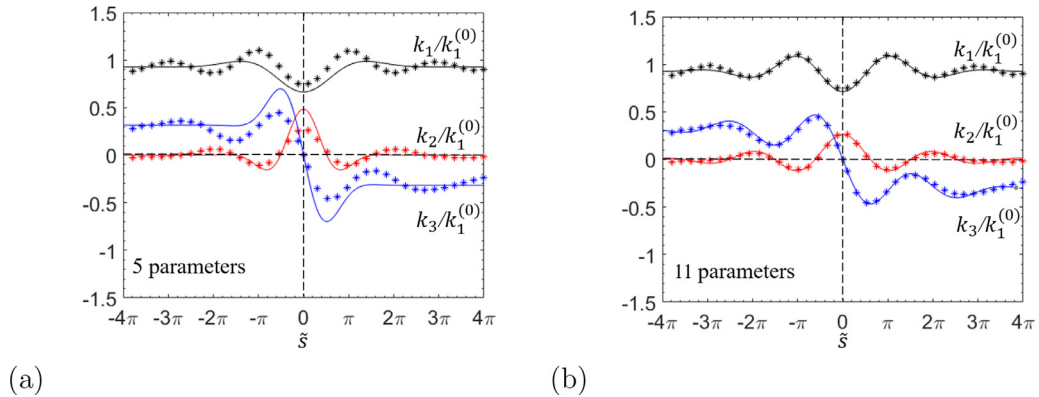


Fig. 9. Rayleigh-Ritz solution (solid line) (a) using Eqs. (15)–(17) with five parameters, and (b) using Eqs. (19)–(21) with eleven parameters, compared with finite-element results (points) for $h/L = 0.32$. The numerical uncertainties in these plots are smaller than the data points.

An improved fit at these lower values of h/L can be obtained by using a trial function with more degrees of freedom. For example, Fig. 9(b) shows the fit using the expressions

$$\tilde{k}_1 = a_{11} \exp(-b_{11}\tilde{s}^2) \cos(c_{11}\tilde{s}) + a_{12} \exp(-b_{12}\tilde{s}^2) \cos(c_{12}\tilde{s}) + \tilde{k}_1^{\text{helix}}(\hat{h}) \quad (19)$$

$$\tilde{k}_2 = a_{21} \exp(-b_{21}\tilde{s}^2) \cos(c_{21}\tilde{s}) + a_{22} \exp(-b_{22}\tilde{s}^2) \cos(c_{22}\tilde{s}) \quad (20)$$

$$\tilde{k}_3(\tilde{s}) = -\frac{3}{2} \int_0^{\tilde{s}} \tilde{k}_2(\tilde{s}) d\tilde{s}. \quad (21)$$

As with Eqs. (15)–(17), we can eliminate one parameter by enforcing the condition that $\tilde{k}_3(\tilde{s}) \rightarrow \tilde{k}_3^{\text{helix}}(\hat{h})$ as $|\tilde{s}| \rightarrow \infty$.

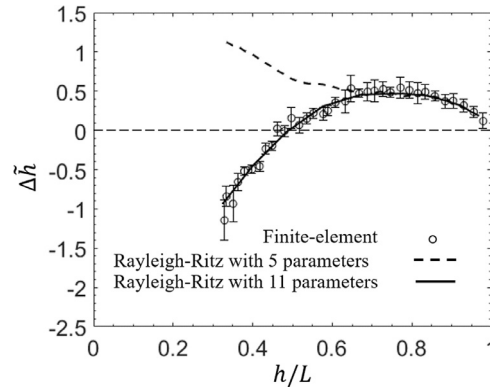


Fig. 10. The change in normalized end-to-end distance $\Delta\tilde{h} = k_1^{(0)} \Delta h$ between a pure helix and a coil with a perversion, showing results obtained by both finite-element calculations and the Rayleigh–Ritz method. The introduction of a perversion causes shrinkage of the fiber if h/L is less than about 0.5. It should also be noted that the 5-parameter Rayleigh–Ritz solution works very well for values of h/L greater than about 0.7.

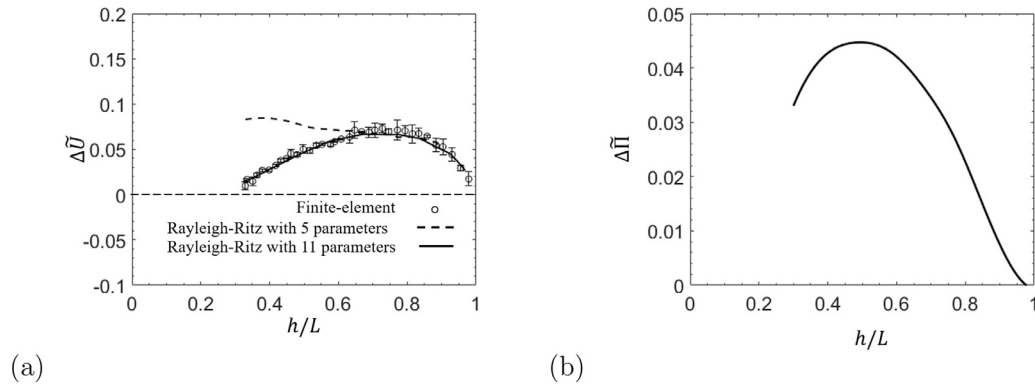


Fig. 11. (a) The difference in strain energy between a purely helical portion of the fiber and the same length of fiber containing a single perversion. Once again, the results are well described by the 5-parameter Rayleigh–Ritz approximation of Eqs. (15)–(17) for $0.65 < h/L < 1$, and by the 11-parameter approximation below this range. (b) The difference in total energy between a purely helical portion of the fiber and the same length of fiber containing a single perversion. This plot is calculated using the 11-parameter Rayleigh–Ritz solution.

3.2. Energetic considerations

One of the obvious questions that arises when considering the introduction of perversions into a coil, is whether the introduction of perversions is energetically favorable or not. In this context, it is important to appreciate that the key concept as to whether a defect such as a perversion is introduced into a body is always the change in total energy, $\Delta\Pi$, rather than the change in strain energy, ΔU . In this particular situation the number of helical coils in the fiber is generally going to be sufficiently large for them to control the relation between the end-to-end length and the force. This means that even if the remote ends of the fiber are subject to displacement-control, the local process of introducing a perversion must be considered as occurring under force-control. The energy penalty associated with the introduction of a perversion must include a potential-energy term, with the change in total energy being given by $\Delta\Pi = \Delta U - P\Delta h$, where Δh is the change in end-to-end length associated with the introduction of a perversion. To explore this expression, we evaluated the difference between the properties of a fiber segment containing a perversion and those of a segment of equal length but in the form of a pure helix. The asymptotic behavior exhibited by Figs. 7 and 9 shows that these differences can be evaluated by integrating over a modest region of the fiber near the perversion.

The first question we addressed was the difference in the end-to-end length of a fiber associated with the introduction of a perversion, Δh . This is plotted in Fig. 10, in which Δh is normalized by the intrinsic curvature, i.e., $\Delta\tilde{h} = k_1^{(0)} \Delta h$. This calculation was performed numerically, and by using both the 5-parameter and the 11-parameter Rayleigh–Ritz approximation. As can be seen in this figure, the 5-parameter approximation provides an excellent description of the shape for $h/L \geq 0.7$, while the 11-parameter approximation provides an excellent description of the shape down to at least $h/L > 0.3$. The important thing to note from this plot is that while the introduction of a perversion causes an increase in h while $h/L > 0.5$, the introduction of a perversion causes the ends of the fiber to move together when $h/L < 0.5$.

Fig. 11(a) shows the difference in the normalized strain energy, $\Delta\tilde{U}$, between a segment of fiber containing a perversion and one that does not. Again, the plot compares the numerical results with the 5- and 11-parameter approximations,

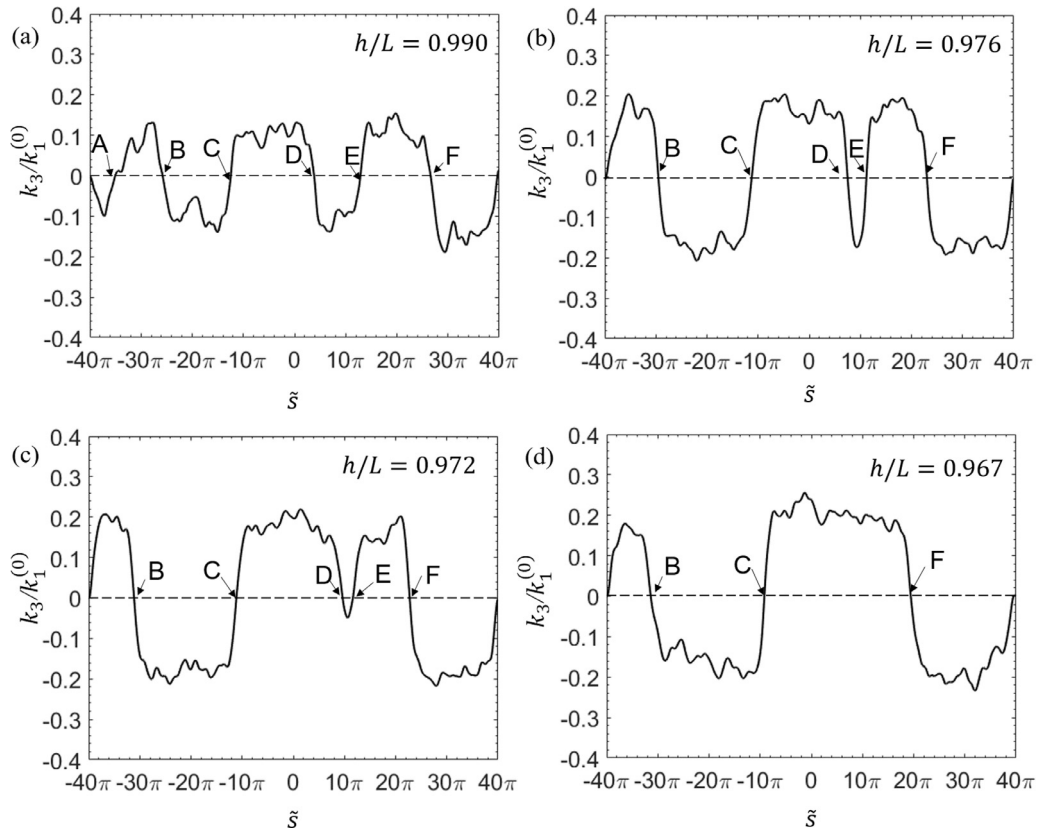


Fig. 12. Perversions are identified by sign changes in $\tilde{k}_3(\tilde{s})$. Those at A D and E are annihilated as h/L is reduced.

showing the agreement of each being in the same range as before. It will be noted that Fig. 11(a) shows that the introduction of a perversion always increases the strain energy in the range $h/L > 0.325$ over which it was feasible to do the numerical calculations, but it also indicates that the strain-energy change may be negative if $h/L < 0.3$. However, as discussed above, it is not the change in strain energy that controls the energetics of introducing a perversion, but the change in total energy. Fig. 10 indicates that the potential energy change associated with the introduction of a perversion is positive when $h/L < 0.5$. This effect is bigger than any negative change in the strain energy, resulting in the plot of Fig. 11(b) for the change in total energy. From this plot we can conclude that a perversion is energetically unfavorable for all values of h/L .

4. Persistence of perversions

Fig. 11(b) shows that there is always a positive energy cost associated with a perversion, suggesting that only geometrically-necessary perversions should be observed. However, it can be seen from this figure that the energy cost is small when the fiber is almost straight (h/L very close to unity). In practice, this means that there is a range of h/L where the energy costs of a perversion can be small compared to numerical or experimental noise. This can lead to the generation of additional perversions. In this section, we explore the persistence of these perversions as h/L is reduced, and the energy cost of the perversions increases.

The formation and persistence of perversions was studied using our finite-element code to generate examples of coiled fibers. Before presenting the results we first note from Fig. 7 (for example) that \tilde{k}_1 and \tilde{k}_2 experience an excursion at a perversion, but then return to the original helix value, whereas \tilde{k}_3 changes sign, because a perversion separates two segments of opposite chiralities. In more complex morphologies, a perversion is therefore most easily characterized by a change in sign in the twist \tilde{k}_3 , so in this section we plot this parameter as a function of distance along the fiber length.

Fig. 12 shows a typical progression of a finite-element plot of \tilde{k}_3 for a fiber of length $L = 80\pi/k_1^{(0)}$ (i.e., a fiber that would present 40 plane coils if the ends were unloaded) as h/L is reduced from 1 to 0.967. Additional perversions, beyond the single geometrically necessary one, were formed in this case, because a much longer fiber was used than for the earlier results, probably allowing some entropic effects to play a role. In the first plot for $h/L = 0.990$, sign changes for \tilde{k}_3 , representing perversions, can be identified at the points A, B, C, D, E and F. The noise associated with the numerical algorithm can be seen in this plot, and when $h/L \approx 1$ the variation associated with noise was similar to that associated with a perversion;

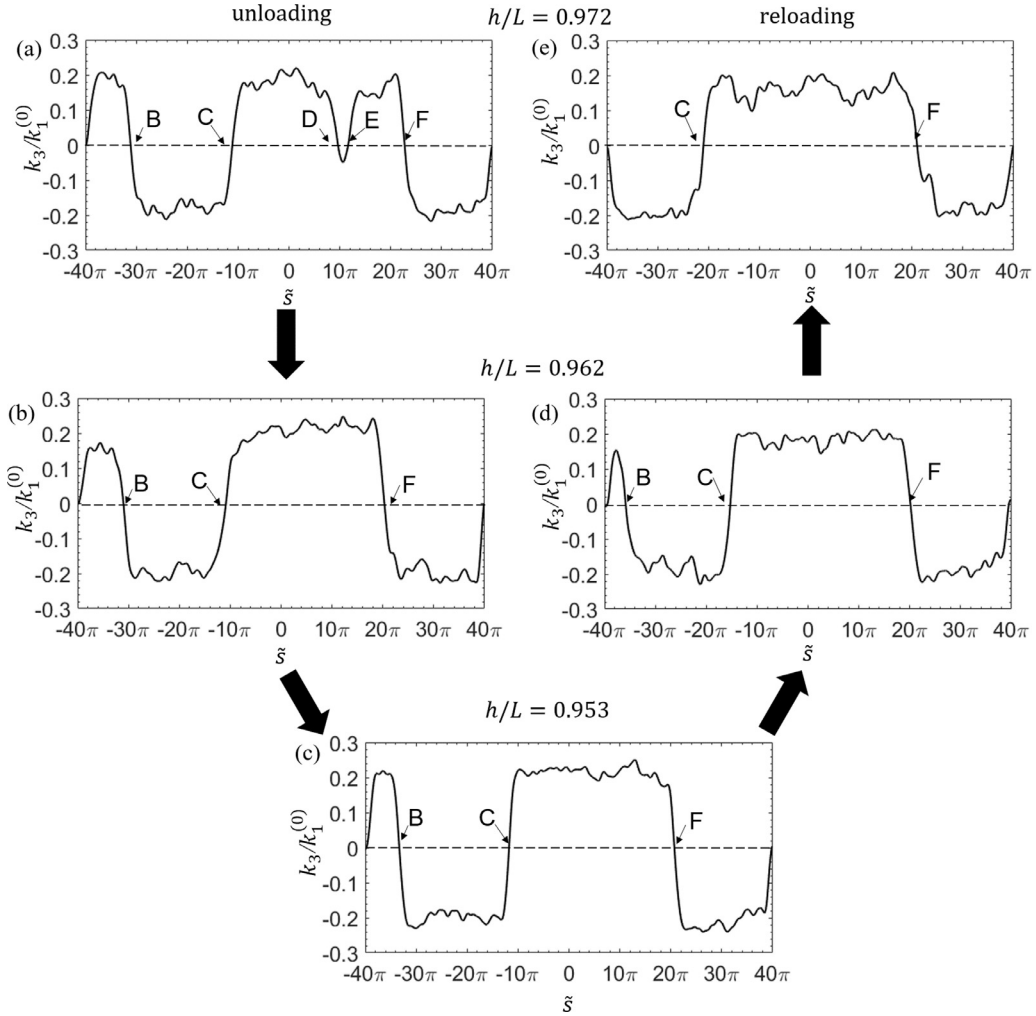


Fig. 13. Evolution of perversions during unloading to $h/L = 0.953$ followed by reloading to $h/L = 0.972$. Notice that perversions D and E are not regenerated during reloading, and B moves to the left-hand end and disappears.

this is the stage at which perversions were generated. Fig. 12(b)–(d) show the evolution of the pattern as h/L is reduced. The perversion at A moves to the end of the fiber and has disappeared at $h/L = 0.976$. The ‘opposite’ perversions at D and E move closer together as the fiber is relaxed. They have annihilated each other (Liu et al., 2016) by the time $h/L = 0.967$. However, if h/L is reduced further, down to $h/L = 0.40$, no further annihilation is observed, even though the energetically optimal solution would involve only a single perversion.

When two perversions are widely separated (i.e., beyond the range in which they interact), there is no energetic advantage in their moving together, so they are expected to persist under unloading. The process of reaching the most energetically favorable state is also impeded by the fact that the net twist, and hence the area under the curves in Fig. 12, must be zero. Thus, for example, B and C cannot simply move closer together in Fig. 12(d) without a corresponding motion of F, since otherwise this would increase the net area under the curve. Notice that when D and E annihilate each other in passing from Fig. 12(a)–(d), there is a corresponding motion of F to the left, to preserve the zero-net-twist condition.

Reloading

Fig. 13 shows the evolution of $\tilde{k}_3(\tilde{s})$ for the same fiber as h/L is decreased from 0.972 to 0.953, and then increased again to 0.972. Notice that the perversions D and E in Fig. 13(a) are not regenerated on reloading, and indeed the perversion at B moves towards the left end and has disappeared by the time h/L returns to 0.972 in Fig. 13(e). Thus, the fiber morphology exhibits significant loading-history dependence.

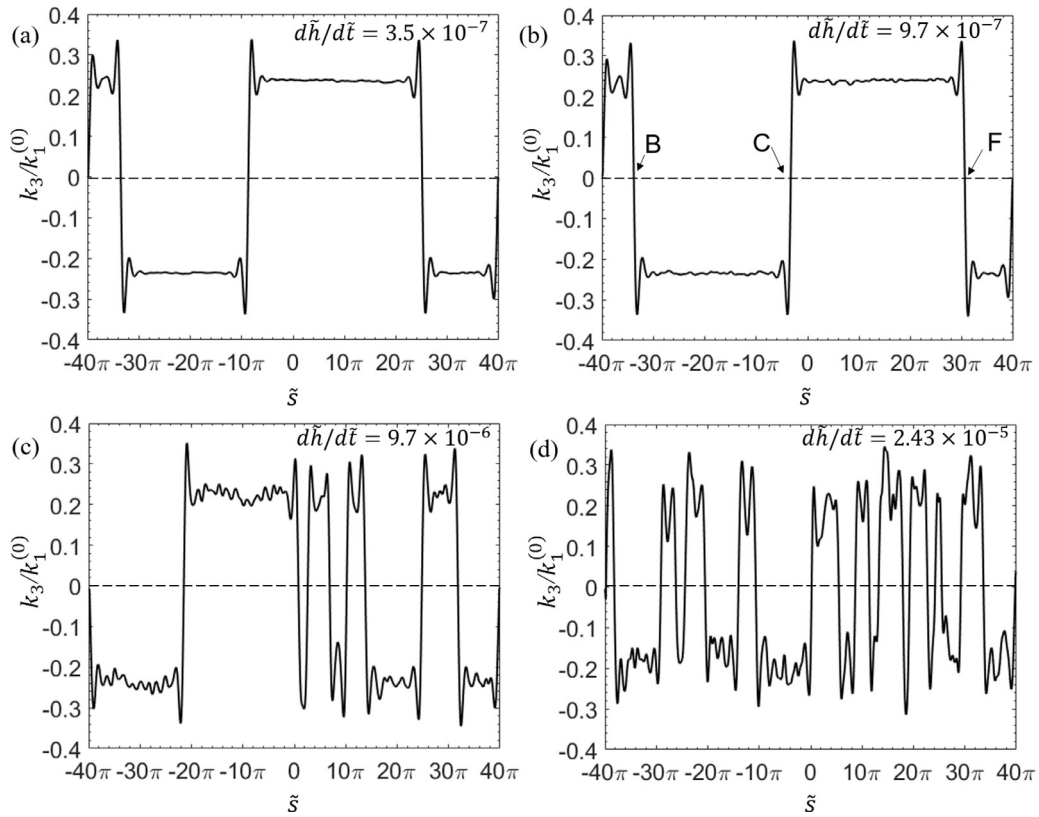


Fig. 14. The velocity at which the ends of the fiber are relaxed influences the number of perversions that are retained at $h/L = 0.5$. $d\tilde{h}/d\tilde{t} =$ (a) 3.5×10^{-7} , (b) 9.7×10^{-7} , (c) 9.7×10^{-6} and (d) 2.43×10^{-5} . Notice that (b) corresponds to the conditions under which Fig. 12 was obtained, and the perversions B, C and F have been retained down to $h/L = 0.5$.

Effects of noise and quenching

The numerical results presented so far in this paper can be thought of as having been obtained under quasi-static conditions, but with enough noise to generate perversions when the fiber is almost straight and the energy barrier is low. This raises the possibility of a potentially interesting future study of how these topological defects might be influenced by noise, and whether there are any analogies to the effects of temperature for defects in materials. Although a detailed study is beyond the scope of this present paper, we present some preliminary observations.

The first set of studies were done to look at the effect of what might be an analogy to quenching. In this context, quenching can be thought of in the following terms. When h/L is close to 1, the energetic distinction between the helical coils and perversions is small, and the probability of forming multiple perversions is high. As h/L is reduced, the energy penalty of a perversion is increased, but co-ordinated motion of the defects is needed for them to annihilate each other. Quenching would correspond to a relaxation rate at which the perversions formed when $h/L \approx 1$ are effectively frozen into the fiber.

The effect of quenching was explored by varying $d\tilde{h}/d\tilde{t}$ over about two orders of magnitude, between 3.50×10^{-7} and 2.43×10^{-5} . The corresponding results for the distributions of k_3 for $h/L = 0.5$ are shown in Fig. 14. It was noted that at the lower speeds corresponding to quasi-static conditions, the number of perversions formed seemed to be constant, although the location of the defects varied slightly. Unfortunately, numerical limitations associated with computational time prevented exploring whether three perversions is an asymptotic limit for this length of fiber for quasi-static conditions, or if a single perversion might ever be formed at slow-enough relaxation rates. However, it can be seen unambiguously that rapid relaxation results in many more perversions, and the number of defects increases with relaxation rate.

Having shown that quenching appears to result in additional defects being frozen into the structure, the second question that arises is whether these can be annealed by mechanical oscillations, which might be an analogy of temperature. The effects of vibration were explored by imposing an oscillating displacement on one end of the fiber after it had been relaxed to $h/L = 0.5$ at different speeds. The results suggested that a sufficiently strong mechanical vibration could induce the perversions to move and to annihilate each other, but no obvious consistency between the magnitude of the oscillations and the resultant defect density was observed.

5. Conclusions

We have investigated the generation and evolution of perversions between helical segments of a fiber with uniform intrinsic curvature when the ends are restrained against rotation. The twist function $\tilde{k}_3(\xi)$ changes sign in passing through a perversion, and this provides a convenient way to identify and approximate the morphology in more complex situations.

The shape of an isolated perversion is well approximated by a simple Rayleigh–Ritz trial function, and this method also gives accurate results for the associated changes in strain energy and end-to-end length, with a considerable saving in computational time relative to a direct finite-element solution.

The lowest energy state is one in which perversions occur only when they are geometrically necessary because of the end restraint against rotation. However, the energy differential is small when the fiber is almost straight, so additional perversions may be introduced by noise in the early stages of unloading when the fiber is almost straight. If the fiber is further unloaded, perversion pairs may approach and annihilate each other, but if the perversions are too far from each other or from the fiber ends, an effective energy barrier exists so that they may persist well below the loading conditions where the energy differential is significant. A sufficiently rapid unloading resulted in a higher density of perversions being frozen into the fiber, than that obtained by slower rates of unloading, suggesting an analogy to the retention of defects in solids after thermal quenching.

Declaration of Competing Interest

The authors declare that they have no known competing financial interests or personal relationships that could have appeared to influence the work reported in this paper.

CRediT authorship contribution statement

Dandan Wang: Conceptualization, Methodology, Software, Data curation, Writing - original draft, Visualization, Investigation. **M.D. Thouless:** Conceptualization, Supervision, Methodology, Writing - original draft, Writing - review & editing, Project administration, Funding acquisition. **Wei Lu:** Conceptualization, Supervision, Writing - review & editing, Project administration, Funding acquisition. **J.R. Barber:** Conceptualization, Methodology, Supervision, Writing - original draft, Visualization, Investigation, Writing - review & editing, Project administration, Funding acquisition.

Acknowledgements

The authors are grateful for financial support from The Procter and Gamble Company.

References

- Arsenlis, A., Parks, D.M., 1999. Crystallographic aspects of geometrically-necessary and statistically-stored dislocation density. *Acta Mater.* 47 (5), 1597–1611.
- Callan-Jones, A.C., Brun, P.T., Audoly, B., 2012. Self-similar curling of a naturally curved elastica. *Phys. Rev. Lett.* 108 (17), 174302.
- Domokos, G., Healey, T.J., 2005. Multiple helical perversions of finite, intrinsically curved rods. *Int. J. Bifur. Chaos* 15 (3), 871–890.
- Gao, P.X., Ding, Y., Mai, W., Hughes, W.L., Lao, C., Wang, Z.L., 2005. Conversion of zinc oxide nanobelts into superlattice-structured nanohelices. *Science* 309 (5741), 1700–1704.
- Gerbode, S.J., Puzey, J.R., McCormick, A.G., Mahadevan, L., 2012. How the cucumber tendril coils and overwinds. *Science* 337 (6098), 1087–1091.
- Goriely, A., 2017. *The mathematics and mechanics of biological growth*, 45. Springer.
- Goriely, A., Tabor, M., 1996. New amplitude equations for thin elastic rods. *Phys. Rev. Lett.* 77, 3537–3540.
- Goriely, A., Tabor, M., 1997. Nonlinear dynamics of filaments i. dynamical instabilities. *Physica D* 105 (1), 20–44.
- Goriely, A., Tabor, M., 1998. Spontaneous helix hand reversal and tendril perversion in climbing plants. *Phys. Rev. Lett.* 80 (7), 1564–1567.
- Goyal, S., Perkins, N.C., Lee, C.L., 2005. Nonlinear dynamics and loop formation in kirchhoff rods with implications to the mechanics of dna and cables. *J. Comput. Phys.* 209 (1), 371–389.
- van der Heijden, G.H.M., Neukirch, S., Goss, V.G.A., Thompson, J.M.T., 2003. Instability and self-contact phenomena in the writhing of clamped rods. *Int. J. Mech. Sci.* 45 (1), 161–196.
- Joos, B., Duesbery, M., 1997. The peierls stress of dislocations: an analytic formula. *Phys. Rev. Lett.* 78 (2), 266.
- Kumar, A., Healey, T.J., 2010. A generalized computational approach to stability of static equilibria of nonlinearly elastic rods in the presence of constraints. *Comput. Methods Appl. Mech. Eng.* 199 (25–28), 1805–1815.
- Liu, S., Yao, Z., Chiou, K., Stupp, S.I., De La Cruz, M.O., 2016. Emergent perversions in the buckling of heterogeneous elastic strips. *Proc. Natl. Acad. Sci.* 113 (26), 7100–7105.
- McMillen, T., Goriely, A., 2002. Tendril perversion in intrinsically curved rods. *J. Nonlinear Sci.* 12 (3), 241–281.
- Mendelson, N.H., 1978. Helical bacillus subtilis macrofibers: morphogenesis of a bacterial multicellular macroorganism. *Proc. Natl. Acad. Sci.* 75 (5), 2478–2482.
- Nye, J.F., 1953. Some geometrical relations in dislocated crystals. *Acta Metall.* 1 (2), 153–162.
- Olson, S.D., Lim, S., Cortez, R., 2013. Modeling the dynamics of an elastic rod with intrinsic curvature and twist using a regularized stokes formulation. *J. Comput. Phys.* 238, 169–187.
- O'Neill, B., 2006. *Elementary Differential Geometry*. Elsevier.
- Pieranski, P., Baranska, J., Skjeltorp, A., 2004. Tendril perversion – a physical implication of the topological conservation law. *Eur. J. Phys.* 25, 613–621.
- Savin, T., Kurpios, N.A., Shyer, A.E., Florescu, P., Liang, H., Mahadevan, L., Tabin, C.J., 2011. On the growth and form of the gut. *Nature* 476 (7358), 57–62.
- Wang, D., Thouless, M.D., Lu, W., Barber, J.R., 2019. In-situ observations of abrasion mechanisms of nonwoven fabric. *Wear* 432, 202945.
- Wang, J., Wang, G., Feng, X., Kitamura, T., Kang, Y., Yu, S., Qin, Q., 2013. Hierarchical chirality transfer in the growth of towel gourd tendrils. *Sci. Rep.* 3, 3102.
- Wie, J.J., Lee, K.M., Ware, T.H., White, T.J., 2015. Twists and turns in glassy, liquid crystalline polymer networks. *Macromolecules* 48 (4), 1087–1092.
- Yang, Y., Zhang, Y., Wei, Z., 2013. Supramolecular helices: chirality transfer from conjugated molecules to structures. *Adv. Mater.* 25 (42), 6039–6049.